Table 1 Relative orbital elements of 1998 WW31 binary system

	All observations	HST only	Charon
Period (days)	574 (10)	521 (133)	6.3872
Semi-major axis (km)	22,300 (800)	21,200 (2,400)	19,366
Eccentricity	0.817 (0.05)	0.800 (0.10)	0.0076
Inclination (degrees)	41.7 (7)	43.8 (10)	96.16
Node longitude (degrees)	94.3 (8)	94.6 (10)	223.0
Pericentre longitude (degrees)	253.8 (7)	251.8 (9)	
Mean longitude at epoch (degrees)	43.4 (4)	48.7 (16)	
Epoch (Julian date)	2,452,300.5	2,452,300.5	
R band magnitudes			
Pair	23.6		
A	24.2		
B	24.6		
Same albedo			
Diameter ratio	1.2		
Mass ratio	1.74		
Same density 2.0 g cm^{-3} (similar to Pluto)			
Diameters (A, B)	118 km, 98 km		
Albedo	0.086 (0.007)		
Same density 1.5 g cm^{-3}			
Diameters (A, B)	129 km, 108 km		
Albedo	0.071 (0.006)		
Same density 1.0 g cm^{-3}			
Diameters (A, B)	148 km, 123 km		
Albedo	0.054 (0.005)		

The orbital elements (mean equator and equinox of J2000.0) of the secondary component, B, of the 1998 WW31 system with respect to its primary, A. (Formal uncertainties in brackets are based on the uncertainties assigned to the individual measurements used as outlined in Fig. 3.) Also shown are the physical properties of the 1998 WW31 components derived from the mass of the system as determined from the orbital parameters (period and semi-major axis), for various assumptions on their density. The orbital elements based only on the HST data are shown to stress the importance of the ground observations in spite of their poorer quality. Charon's elements are from ref. 14.

semi-major axis; however, even the values presented in this paper are accurate enough to lead to a good estimate of the mass of the system.

The orbit is not determined well enough to predict with precision when mutual eclipses could happen. With the present solution, eclipses could take place in 2055 or 2056. The HST observations scheduled for the next opposition will allow a better prediction of when mutual events will occur.

Using both ground-based and HST observations, the two components are found to have a magnitude difference in R band of 0.4 and a total magnitude of 23.6. If we assume that they have the same albedo, their diameter ratio is 1.2. If they have the same density, it is possible to get the mass of each component. The diameters can be estimated assuming a given density. An albedo can then be derived from the observed magnitude and the estimated diameter. Table 1 summarizes the results obtained assuming various densities from 1 to 2 gm cm^{-3} (Pluto's density is about 2 gm cm^{-3}). The associated albedo values are in the range 0.05 to 0.08. The albedo of cometary nuclei, 0.04 (ref. 19), is the value generally assumed and used for KBO size estimation; however, if we use that low albedo value for 1998 WW31, then the KBO would have a very low density of roughly 1 gm cm^{-3}, considerably less than the density of Pluto.

The announcement of the binarity of 1998 WW31 was the first of what has become a series of binary KBO discoveries. Within less than a year after our announcement of the binarity of 1998 WW31, six other KBOs have been discovered to be binaries: 2001 QT297 (ref. 20) and 2001 QW322 (ref. 21) using ground-based observations, and 1999 TC36 (ref. 22), (26308) 1998 SM165 (ref. 23), 1997 CQ29 (ref. 24), and 2000 CF105 (ref. 25) using HST. We now know of seven binary systems in a sample of nearly 600 objects. Although we have to be careful when dealing with small numbers, binarity is definitely not uncommon in the Kuiper belt, comprising at least 1% of the currently known KBO population. □

Received 5 December 2001; accepted 27 February 2002.

1. Chapman, C. R. *et al.* Discovery and physical properties of Dactyl, a satellite of asteroid 243 Ida. *Nature* **374,** 783–785 (1995).
2. Belton, M. J. S. *et al.* The discovery and orbit of 1993 (243)1 Dactyl. *Icarus* **120,** 185–199 (1995).
3. Margot, J. L. *et al.* Satellites of minor planets. *IAU Circ.* 7503 (2000).
4. Benner, L. A. M. *et al.* 1999_KW4. *IAU Circ.* 7632 (2001).
5. Nolan, M. C. *et al.* 2000_UG11. *IAU Circ.* 7632 (2000).
6. Merline, W. J. *et al.* Discovery of a moon orbiting the asteroid 45 Eugenia. *Nature* **401,** 565–567 (1999).
7. Merline, W. J. *et al.* Discovery of companions to asteroids 762 Pulcova and 90 Antiope by direct imaging. DPS Meeting 32, abstr. no. 13.06 (American Astronomical Society, 2000).
8. Brown, M. E. & Margot, J. L. S/2001 (87) 1. *IAU Circ.* 7588 (2001).
9. Merline, W. J. *et al.*; Margot, J. L. & Brown, M. E. S/2001 (22) 1. *IAU Circ.* 7703 (2001).
10. Merline, W. J. *et al.* S/2002 (3749) 1. *IAU Circ.* 7827 (2002).
11. Merline, W. J. *et al.* S/2001 (617) 1. *IAU Circ.* 7741 (2001).
12. Duncan, M., Quinn, T. & Tremaine, S. The origin of short-period comets. *Astrophys. J.* **328,** L69–L73 (1988).
13. Jewitt, D. C. & Luu, J. X. 1992 QB1. *IAU Circ. 5611* (1992).
14. Millis, R. L. *et al.* 1998 WW31. *Minor Planet Electron. Circ. 1999-B24* (2001).
15. Veillet, C. *et al.* 1998 WW31. *Minor Planet Electron. Circ. 2001-G29* (2001).
16. Holtzman, J. *et al.* The performance and calibration of WFPC2 on the Hubble Space Telescope. *Publ. Astron. Soc. Pacif.* **107,** 156–178 (1995).
17. Image Reduction and Analysis Facility. ⟨http://iraf.noao.edu⟩.
18. Tholen, D. J. & Buie, M. W. The orbit of Charon. *Icarus* **125,** 245–260 (1997).
19. Jewitt, D., Aussel, H. & Evans, A. The size and albedo of the Kuiper-belt object (20000) Varuna. *Nature* **411,** 446–447 (2001).
20. Elliot, J. L., Kern, S. D., Osip, D. J. & Burles, S. M. 2001 QT_297. *IAU Circ. 7733* (2001).
21. Kavelaars, J. J. *et al.* 2001 WQ_322. *IAU Circ. 7749* (2001).
22. Trujillo, C. A. & Brown, M. E. 1999 TC_36. *IAU Circ. 7787* (2001).
23. Brown, M. E. & Trujillo, C. A. (26308) 1998 SM_165. *IAU Circ. 7807* (2001).
24. Noll, K. *et al.* 1997 CQ_29. *IAU Circ. 7824* (2002).
25. Noll, K. *et al.* 2000 CF_105. *IAU Circ.* 7857 (2002).

Acknowledgements

C.V., A.D., D.J.T. and M.C. are visiting astronomers at the Canada-France-Hawaii Telescope (CFHT), operated by the National Research Council of Canada, the Centre National de la Recherche Scientifique of France and the University of Hawaii. J.Wm.P. and M.B. are visiting astronomers at the Kitt Peak National Observatory, National Optical Astronomy Observatory, which is operated by the Association of Universities for Research in Astronomy, Inc. (AURA) under cooperative agreement with the National Science Foundation. This work, supported by funding from NASA, is partly based on observations made with the NASA/ESA Hubble Space Telescope, obtained at the Space Telescope Science Institute, which is operated by AURA under a NASA contract.

Competing interests statement

The authors declare that they have no competing financial interests.

Correspondence and requests for materials should be addressed to C.V. (e-mail: veillet@cfht.hawaii.edu).

Electrical detection of spin precession in a metallic mesoscopic spin valve

F. J. Jedema, H. B. Heersche, A. T. Filip, J. J. A. Baselmans & B. J. van Wees

Department of Applied Physics and Materials Science Center, University of Groningen, Nijenborgh 4.13, 9747 AG Groningen, The Netherlands

To study and control the behaviour of the spins of electrons that are moving through a metal or semiconductor is an outstanding challenge in the field of 'spintronics', where possibilities for new electronic applications based on the spin degree of freedom are currently being explored[1–5]. Recently, electrical control of spin coherence[6] and coherent spin precession during transport[7] was studied by optical techniques in semiconductors. Here we report controlled spin precession of electrically injected and detected electrons in a diffusive metallic conductor, using tunnel barriers in combination with metallic ferromagnetic electrodes as spin injector and detector. The output voltage of our device is sensitive to the spin degree of freedom only, and its sign can be switched from positive to negative, depending on the relative magnetization of the ferromagnetic electrodes. We show that the spin

direction can be controlled by inducing a coherent spin precession caused by an applied perpendicular magnetic field. By inducing an average precession angle of 180°, we are able to reverse the sign of the output voltage.

In our experiment we use a mesoscopic spin valve (Fig. 1a), where a cobalt ferromagnetic electrode (Co1) injects spin-polarized electrons into an aluminium (Al) strip via a tunnel barrier. At a distance L from the injector a second cobalt electrode (Co2) is placed, which detects spin-polarized electrons in the Al strip through a tunnel barrier. The presence of the tunnel barriers is crucial, as they provide a high spin dependent resistance, which enhances the spin polarization of the injected current flowing into the Al strip[8–10]. In addition, the barriers cause the electrons, once injected, to have a negligible probability of losing their spin information by escaping into the Co electrodes. During the time of travel from injector to detector, the spin direction of the electrons can therefore only be altered by (random) spin flip scattering processes in the Al strip or, in the presence of an external magnetic field, by coherent precession. Here we experimentally demonstrate both processes by measuring the amplitude of the spin signal, first as a function of the Co electrode spacing L and second as a function of an applied perpendicular magnetic field. A related method of probing spin injection and detection has been reported by Johnson and Silsbee[3]. However, the reduction of the sample dimensions by 3 orders of magnitude and the introduction of tunnel barriers enables us to observe a clear sign reversal of the output voltage V due to coherent precession, and allows us to make direct comparison with theory.

We made a batch of 10 devices with L ranging from 550 to 1,350 nm, using a suspended shadow mask evaporation process[11] and electron beam lithography for patterning (Fig. 1a). In the first step, an Al strip with a thickness of 50 nm and a width of 250 nm is evaporated on a thermally oxidized silicon substrate by electron-gun evaporation. Next, the Al strip is exposed to an oxygen (O_2) environment of 5×10^{-3} mbar for 10 minutes, producing a thin aluminium oxide (Al_2O_3) layer. In the third step, without breaking the vacuum, we evaporate two ferromagnetic Co electrodes with sizes of $0.4 \times 4\,\mu m^2$ (Co1) and $0.2 \times 12\,\mu m^2$ (Co2) and a thickness of 50 nm. Two $Al/Al_2O_3/Co$ tunnel junctions are thus formed at the overlap of the Co electrodes and the Al strip (Fig. 1b). The conductivity of the Al film was measured to be $\sigma_{Al} = 1.1 \times 10^7\,\Omega^{-1}\,m^{-1}$ at room temperature and $\sigma_{Al} = 1.7 \times 10^7\,\Omega^{-1}\,m^{-1}$ at 4.2 K. The resistance of the tunnel barriers was determined to be typically 600 Ω of the Co1 electrode and 1,200 Ω for the Co2 electrode at room temperature, both increasing by 10% at 4.2 K. Different geometric aspect ratios of Co1 and Co2 are used to obtain different coercive fields. This allows us to control their relative magnetization configuration (parallel/antiparallel) by sweeping an applied magnetic field B, directed parallel to their long axes[4].

The spin polarization P of the current I injected from the Co1 electrode into the Al strip is determined by the ratio of the different spin-up and spin-down tunnel barrier resistances $R_\uparrow$ and $R_\downarrow$, and in first order can be written[12] as $P = (N_\uparrow - N_\downarrow)/(N_\uparrow + N_\downarrow)$. Here $N_\uparrow(N_\downarrow)$ is the spin-up (spin-down) density of states at the Fermi level of the electrons in the Co electrodes. The injected spin current

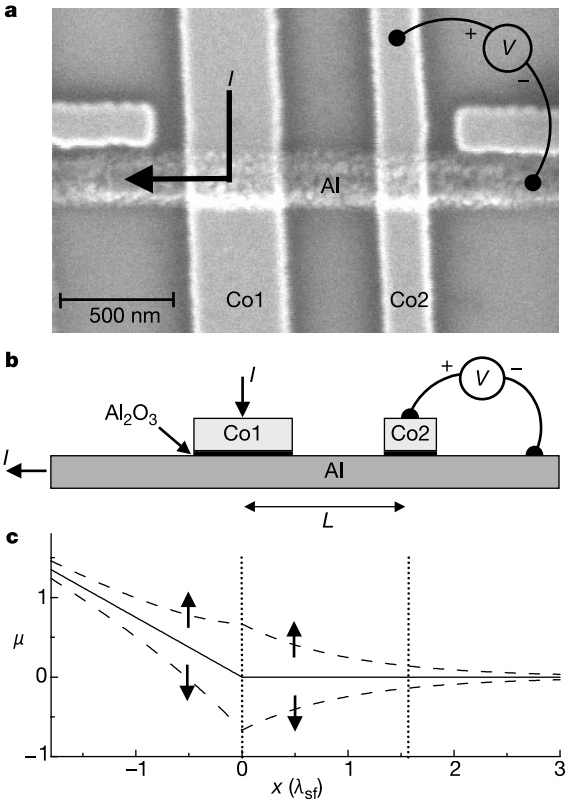

Figure 1 Geometry of our spin valve device. **a**, Scanning electron microscope image of a device with a cobalt (Co) electrode spacing of $L = 650$ nm. Current is sent from Co1 into the Al strip. The voltage is measured between Co2 and the right side of the Al strip. **b**. Device cross-section. **c**, The spatial dependence of the spin-up and spin-down electrochemical potentials (μ, dashed lines) in the Al strip. The solid lines indicate the electrochemical potential (voltage) of the electrons in the absence of spin injection. λ_{sf}, spin flip length.

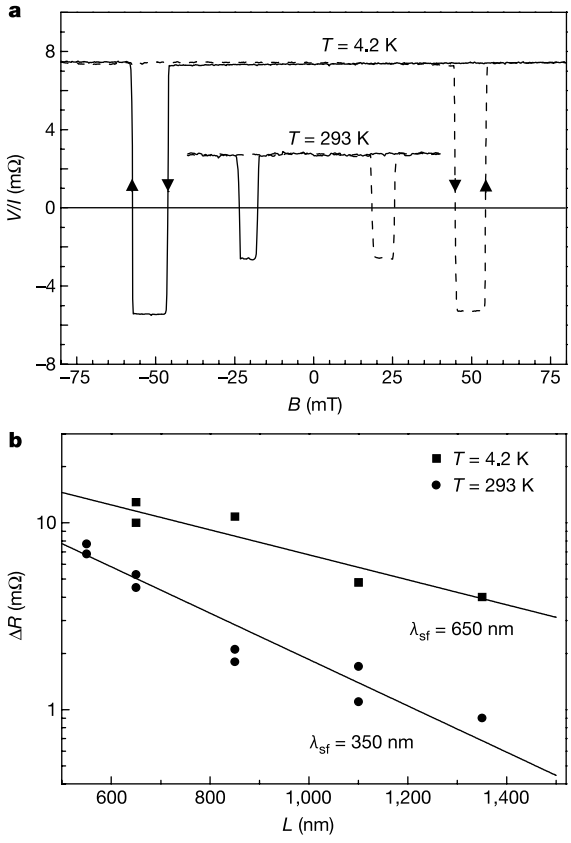

Figure 2 Spin valve effect. **a**, Output signal V/I as a function of the in-plane magnetic field B for a sample with a Co electrode spacing $L = 650$ nm at $T = 4.2$ K and room temperature. The solid (dashed) lines correspond to the negative (positive) sweep direction. **b**, The dependence of the spin-dependent resistance ΔR on the Co electrode spacing L at $T = 4.2$ K and room temperature. The solid squares represent data taken at $T = 4.2$ K, the solid circles are taken at room temperature. The solid lines represent the best fits based on equation (1).

causes the densities (or electrochemical potentials) of the spin-up and spin-down electrons in the Al strip to become unequal (Fig. 1c). This unbalance is transported to the Co2 detector electrode by diffusion, and can therefore be detected. Owing to the spin-dependent tunnel barrier resistances, the Co2 electrode detects a weighted average of the two spin densities, which causes the detected output voltage V to be proportional to P^2.

Figure 2a shows a typical output signal V/I as a function of an in-plane magnetic field B, directed parallel to the long axes of Co1 and Co2, taken at room temperature and 4.2 K. The measurements are performed by standard a.c. lock-in techniques, using a current $I = 100\,\mu$A. Sweeping the magnetic field from negative to positive, a sign reversal of the output signal is observed, when the magnetization of Co1 flips at 19 mT (room temperature) and 45 mT (4.2 K), and the device switches from a parallel to antiparallel configuration. When the magnetization of Co2 flips at 25 mT (room temperature) and 55 mT (4.2 K), the magnetizations are parallel again, but now point in the opposite direction. The fact that the output signal switches symmetrically around zero indicates that this experiment is sensitive to the spin degree of freedom only.

We have calculated the expected magnitude of the output signal V/I as a function of the Co electrode spacing L by solving the spin coupled diffusion equations for the spin-up and spin-down electrons in the Al strip[13–15]. Taking into account the fact that the tunnel barrier resistances are much larger than the resistance of the Al strip over a spin flip length, we obtain:

$$\frac{V}{I} = \pm\frac{1}{2}P^2\frac{\lambda_{sf}}{\sigma_{Al}A}\exp(-L/\lambda_{sf}) \qquad (1)$$

where $\lambda_{sf} = \sqrt{D\tau_{sf}}$ is the spin flip length, A the cross-sectional area, D the diffusion constant, and τ_{sf} the spin flip time of the Al strip. The positive (negative) sign corresponds to a parallel (antiparallel) magnetization configuration of the Co electrodes.

Figure 2b shows the measured spin dependent resistance $\Delta R = \Delta V/I$ as a function of L, where ΔV is the output voltage difference between parallel and antiparallel configuration. By fitting the data to equation (1), we find $P = 0.11 \pm 0.02$ at both 4.2 K and room temperature, $\lambda_{sf} = 650 \pm 100$ nm at 4.2 K and $\lambda_{sf} = 350 \pm 50$ nm at room temperature. The diffusion constant D is calculated using the Einstein relation $\sigma_{Al} = e^2 N_{Al} D$, where e is the electron charge and $N_{Al} = 2.4 \times 10^{22}$ states per eV per cm^3 is the density of states of Al at the Fermi energy[16]. Using $D = 4.3 \times 10^{-3}$ m^2 s^{-1} at 4.2 K and $D = 2.7 \times 10^{-3}$ m^2 s^{-1} at room temperature, we obtain $\tau_{sf} = 100$ ps at 4.2 K and $\tau_{sf} = 45$ ps at room temperature. These values are in good agreement with those reported in the literature[3,17–20].

Having determined the parameters P, λ_{sf} and D, we are now ready to study spin precession of the electron spin during its diffusion time t between Co1 and Co2. In an applied field $B_\perp$, perpendicular to the substrate plane, the injected electron spins in the Al strip precess around an axis parallel to $B_\perp$. This alters the spin direction by an angle $\varphi = \omega_L t$, where $\omega_L = g\mu_B B_\perp/\hbar$ is the Larmor frequency, g is the g-factor of the electron ($\sim$2 for Al), μ_B is the Bohr magneton and $\hbar$ is Planck's constant divided by 2π. Because the Co2 electrode detects the projection of the spin direction φ onto its own magnetization direction (0 or π), the contribution of an electron to

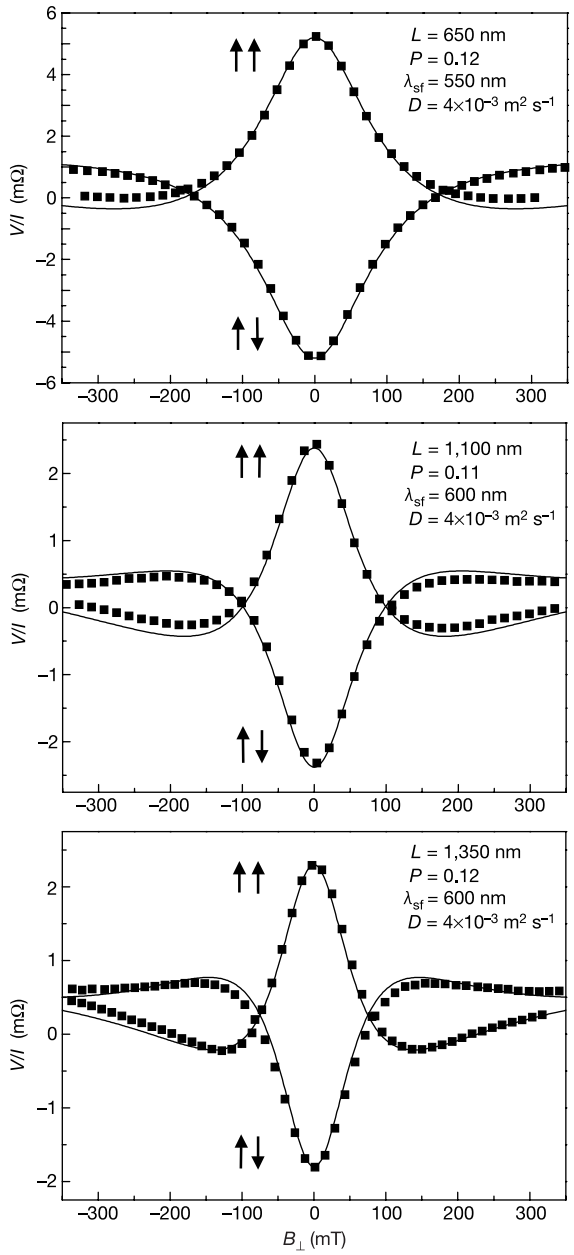

Figure 3 Modulation of the output signal V/I due to spin precession as a function of a perpendicular magnetic field $B_\perp$, for $L = 650$ nm, $L = 1{,}100$ nm and $L = 1{,}350$ nm. The solid squares represent data taken at $T = 4.2$ K, whereas the solid lines represent the best fits based on equations (2) and (3). The arrows indicate the relative magnetization configuration (parallel/antiparallel) of the Co electrodes. P, spin polarization; D, diffusion constant.

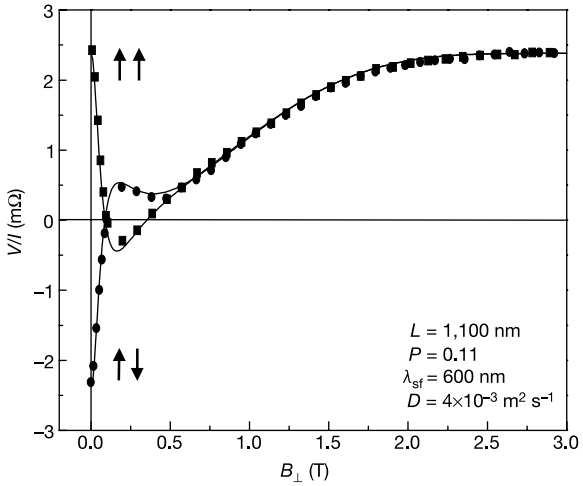

Figure 4 Modulation of the output signal V/I as a function of a perpendicular magnetic field $B_\perp$ up to 3 T, for $L = 1{,}100$ nm. The solid squares/circles represent data taken at $T = 4.2$ K, whereas the solid lines represent the best fit based on equations (2) and (3). The arrows indicate the relative magnetization configuration (parallel/antiparallel) of the Co electrodes.

the output voltage V is proportional to $\pm\cos(\varphi)$. However, in an (infinite) diffusive conductor the diffusion time t from Co1 to Co2 has a broad distribution $P(t) = [1/\sqrt{4\pi Dt}]\exp[-L^2/(4Dt]$, where $P(t)$ is proportional to the number of electrons that, once injected at the Co1 electrode ($x = 0$), arrive at the Co2 electrode ($x = L$) after a diffusion time t. The output voltage V at the Co2 detector electrode as a function of $B_\perp$ is calculated by summing all contributions of the electron spins over all diffusion times t. We obtain:

$$V(B_\perp) = \pm I \frac{P^2}{e^2 N_{Al} A} \int_0^\infty P(t)\cos(\omega_L t)\exp(-t/\tau_{sf})\mathrm{d}t \qquad (2)$$

The exponential factor in equation (2) describes the effect of the spin flip scattering. For $\omega_L = 0$, equation (2) reduces to equation (1). We note that equation (2) can be evaluated analytically, and we have verified that it yields the same result as obtained by Johnson and Silsbee, who explicitly solved the Bloch equations with the appropriate boundary conditions[21,22].

At large $B_\perp$, the magnetization direction of the Co electrodes is tilted out of the substrate plane with an angle ϑ. When we include this effect we calculate:

$$V(B_\perp, \vartheta) = V(B_\perp)\cos^2(\vartheta) + |V(B_\perp = 0)|\sin^2(\vartheta) \qquad (3)$$

Equation (3) shows that with increasing ϑ (from zero), the precession signal is reduced and a positive background output signal appears. For $\vartheta = 0$ equation (3) reduces to equation (2). In the limit that $\vartheta = \pi/2$, the magnetization of the Co electrodes is perpendicular to the substrate plane and parallel to $B_\perp$. No precession now occurs, and the full output signal $|V(B_\perp = 0)|$ is recovered. The angle ϑ has been determined independently as a function of $B_\perp$ by measuring the anisotropic magnetoresistance of the Co electrodes[23].

In Fig. 3 we plot the measured output signal V/I at 4.2 K, as a function of $B_\perp$ for $L = 650$ nm, $L = 1{,}100$ nm and $L = 1{,}350$ nm. Before the measurement an in-plane magnetic field B directed parallel to the long axes of Co electrodes is used to prepare the magnetization configuration of the Co electrodes. For a parallel (antiparallel) configuration we observe an initial positive (negative) signal, which drops in amplitude as $B_\perp$ is increased from zero field. This is called the Hanle effect in ref. 3. The two curves cross where the average angle of precession is about 90° and the output signal is close to zero. As $B_\perp$ is increased beyond this field, we observe that the output signal changes sign and reaches a minimum (maximum) when the average angle of precession is about 180°, thereby effectively converting the injected spin-up population into a spin-down and vice versa. We have fitted the data with equations (2) and (3), as shown in Fig. 3. We find for all measured samples that the best-fit parameters P, λ_{sf} and D are very close to those independently obtained from the length dependence measurements (Fig. 2).

As already visible in Fig. 3, for $B > 200$ mT an asymmetry is observed between the parallel and antiparallel curves. This is due to the fact that magnetization of the Co electrodes does not remain in the substrate plane. In Fig. 4 we plot the measured output signal V/I at $T = 4.2$ K for L=1,100 nm up to $B_\perp = 3$ T, together with the calculated curve, using P, λ_{sf} and D as obtained from the best fit in Fig. 3. The data are in close agreement with equation (3), and show a suppression of the precessional motion of the electron spin. The full magnitude of the output signal is recovered at large $B_\perp$, when $\vartheta = \pi/2$ and no precession takes place. Preliminary results show that precession effects similar to those shown in Fig. 3 can also be obtained at room temperature.

We believe that the system we report here, with its unique sensitivity to the spin degree of freedom, will make possible detailed studies of a variety of spin-dependent transport phenomena. □

Received 18 January; accepted 21 February 2002.

1. Prinz, G. A. Magnetoelectronics. *Science* **282,** 1660–1663 (1998).
2. Wolf, S. A. *et al.* Spintronics: A spin-based electronics vision for the future. *Science* **294,** 1488–1495 (2001).
3. Johnson, M. & Silsbee, R. H. Interfacial charge-spin coupling: Injection and detection of spin magnetization in metals. *Phys. Rev. Lett.* **55,** 1790–1793 (1985).
4. Jedema, F. J., Filip, A. T. & van Wees, B. J. Electrical spin injection and accumulation at room temperature in an all-metal mesoscopic spin valve. *Nature* **410,** 345–348 (2001).
5. Hernando, D. H., Nazarov, Yu. V., Brataas, V. & Bauer, G. E. W. Conductance modulation by spin precession in noncollinear ferromagnet normal-metal ferromagnet systems. *Phys. Rev. B* **62,** 5700–5712 (2000).
6. Salis, G. *et al.* Electrical control of spin coherence in semiconductor nanostructures. *Nature* **414,** 619–622 (2001).
7. Kikkawa, J. M. & Awschalom, D. D. Lateral drag of spin coherence in gallium arsenide. *Nature* **397,** 139–141 (1999).
8. Schmidt, G. *et al.* Fundamental obstacle for electrical spin injection from a ferromagnetic metal into a diffusive semiconductor. *Phys. Rev. B* **62,** R4790–R4793 (2000).
9. Rashba, E. I. Theory of electrical spin injection: Tunnel contacts as a solution of the conductivity mismatch problem. *Phys. Rev. B* **62,** R16267–R16270 (2000).
10. Fert, A. & Jaffrès, H. Conditions for efficient spin injection from a ferromagnetic metal into a semiconductor. *Phys. Rev. B* **64,** 184420–184428 (2001).
11. Jackel, L. D., Howard, R. E., Hu, E. L., Tennant, D. M. & Grabbe, P. 50-nm silicon structures fabricated with trilevel electron beam resist and reactive-ion etching. *Appl. Phys. Lett.* **39,** 268–270 (1981).
12. Julliere, M. Tunneling between ferromagnetic films. *Phys. Lett. A* **54,** 224–227 (1975).
13. Van Son, P., van Kempen, H. & Wyder, P. Boundary resistance of the ferromagnetic-nonferromagnetic metal interface. *Phys. Rev. Lett.* **58,** 2271–2273 (1987).
14. Jedema, F. J., Nijboer, M. S., Filip, A. T. & van Wees, B. J. Spin injection and spin accumulation in permalloy-copper mesoscopic spin valves.Preprint cond-mat/0111092 at ⟨http://xxx.lanl.gov⟩ (2002); *Phys. Rev. B* (submitted).
15. Johnson, M. Spin accumulation in gold films. *Phys. Rev. Lett.* **70,** 2142–2145 (1993).
16. Papaconstantopoulos, D. A. *Handbook of the Band Structure of Elemental Solids* (Plenum, New York, 1986).
17. Meservey, R. & Tedrow, P. M. Surface relaxation times of conduction-electron spins in superconductors and normal metals. *Phys. Rev. Lett.* **41,** 805–808 (1978).
18. Monod, P. & Beneu, F. Conduction-electron spin flip by phonons in metals: Analysis of experimental data. *Phys. Rev. B* **19,** 911–916 (1979).
19. Grimaldi, C. & Fulde, P. Spin-orbit scattering effects on the phonon emission and absorption in superconducting tunneling junctions. *Phys. Rev. Lett.* **77,** 2550–2553 (1996).
20. Fabian, J. & Das Sarma, S. Phonon-induced spin relaxation of conduction electrons in aluminium. *Phys. Rev. Lett.* **83,** 1211–1214 (1999).
21. Johnson, M. & Silsbee, R. H. Coupling of electronic charge and spin at a ferromagnetic-paramagnetic metal interface. *Phys. Rev. B* **37,** 5312–5325 (1988).
22. Johnson, M. & Silsbee, R. H. Spin-injection experiment. *Phys. Rev. B* **73,** 5326–5335 (1988).
23. Rijks, Th. G. S. M., Coehoorn, R., de Jong, M. J. M. & de Jonge, W. J. M. Semiclassical calculations of the anisotropic magnetoresistance of NiFe-based thin films, wires, and multilayers. *Phys. Rev. B* **51,** 283–291 (1995).

Acknowledgements

We thank the Stichting Fundamenteel Onderzoek der Materie (FOM) and NEDO (project 'nano-scale control of magnetoelectronics for device applications') for support.

Competing interests statement

The authors declare that they have no competing financial interests.

Correspondence and requests for materials should be addressed to F.J.J. (e-mail: jedema@phys.rug.nl).

Rapid electroplating of insulators

Vincent Fleury*, Wesley A. Watters*, Levy Allam† & Thierry Devers†

** Laboratoire de Physique de la Matière Condensée, Ecole Polytechnique/CNRS, 91128 Palaiseau cedex, France*
† Laboratoire de Physique Electronique, IUT de Chartres, 1 Place Mendès-France, 28000 Chartres, France

Electrochemical techniques for depositing metal films and coatings[1] have a long history[2–5]. Such techniques essentially fall into two categories, with different advantages and disadvantages. The first, and oldest, makes use of spontaneous redox reactions to deposit a metal from solution, and can be used on both insulating and metallic substrates. But the deposition conditions of these processes are difficult to control *in situ*, in part because of the